9-2020

Nonlinear Optical Measurements of $CdSiP_2$ at Near and Mid-infrared Wavelengths

Manuel R. Ferdinandus
Air Force Institute of Technology

Jamie J. Gengler

Kent L. Averett

Kevin T. Zawilski

Peter G. Schunemann

See next page for additional authors

Research Article | Vol. 10, No. 9 / 1 September 2020 / Optical Materials Express 2066
Optical Materials EXPRESS

Nonlinear optical measurements of $CdSiP_2$ at near and mid-infrared wavelengths

MANUEL R. FERDINANDUS,[1,2,*] JAMIE J. GENGLER,[2,3] KENT L. AVERETT,[2,3] KEVIN T. ZAWILSKI,[4] PETER G. SCHUNEMANN,[4] AND CARL M. LIEBIG[2]

[1]*Department of Engineering Physics, Air Force Institute of Technology, 2950 Hobson Way, Wright-Patterson AFB, OH 45433, USA*
[2]*Materials and Manufacturing Directorate, Air Force Research Laboratory, 2179 12th St., Wright-Patterson AFB, OH 45433, USA*
[3]*UES, Inc., 4401 Dayton - Xenia Rd., Dayton, OH 45432, USA*
[4]*BAE Systems, MER15, Nashua, NH 03061, USA*
[*]*Manuel.Ferdinandus@afit.edu*

Abstract: We measure the birefringence of the nonlinear optical (NLO) properties of cadmium silicon phosphide via the Z-scan technique at near and mid-infrared wavelengths. We discuss the implications of the NLO properties on optical parametric amplifier performance. We find that the nonlinear absorption does reduce the conversion efficiency, while the nonlinear refraction has a negligible effect.

1. Introduction

Recently there has been much interest in the use of cadmium silicon phosphide ($CdSiP_2$ or CSP in this work) for mid-infrared (mid-IR) difference frequency generation (DFG) in optical parametric amplifiers (OPA) [1–4]. This spectral region (3-5 μm) has been recognized as important for communication, remote sensing and directed energy applications due to the wide atmospheric transmission windows that allow for relatively low loss propagation [5,6]. CSP is a tetragonal point group ($\bar{4}2m$) negative uniaxial crystal with a large second order nonlinearity (d_{36} = 84.5 pm/V) with sufficiently large birefringence (−0.05), large band gap (E_g =2.45 eV) for a wide transparency range and lower linear absorption at commonly utilized pumping wavelengths than alternative materials such as $ZnGeP_2$ [7] at the expense of a lower thermal conductivity [8]. The linear and second order nonlinear optical (NLO) properties of CSP have been previously measured [8–10]. In this work, we measure the nonlinear absorption (NLA) and nonlinear refraction (NLR) at pumping wavelengths (1.5 μm and 2.0 μm) in the near-infrared (NIR) as well as select output wavelengths in the mid-IR (3.0 μm through 5.0 μm). We then examine the effects of this NLA and NLR on OPA performance. We show that at high pumping irradiances NLA can be a limiting factor to OPA performance by increasing the absorption of the pump and reducing the conversion efficiency.

2. Experimental procedure

In this work, we utilize the well-known Z-scan technique shown in Fig. 1 to measure the NLO properties from 1.5 μm to 5.0 μm. Z-scan measurements were performed using a Ti:Sapphire amplified system (KM Labs Wyvern 1000-10) producing 4.0 mJ, 35 fs (FWHM) pulses at 790 nm operating at a 1 kHz repetition rate. An optical parametric generator/amplifier (Light Conversion TOPAS-Prime) is pumped by the fundamental to generate 50 fs (FWHM) pulses. The beam was spatially filtered to produce a Gaussian irradiance profile.

#399516 https://doi.org/10.1364/OME.399516
Journal © 2020 Received 4 Jun 2020; revised 22 Jul 2020; accepted 25 Jul 2020; published 5 Aug 2020

Optical Materials EXPRESS

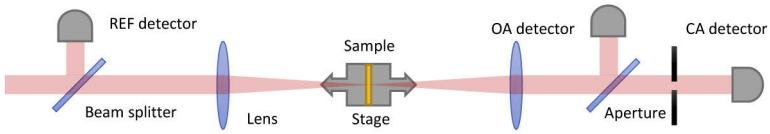

Fig. 1. Z-scan technique. The sample is scanned through the focus of a Gaussian beam. The open aperture (OA) detector measures the total power transmitted and is sensitive to the nonlinear absorption (NLA). The aperture before the closed aperture (CA) detector makes the detector sensitive to the self-focusing/defocusing of the beam and hence the nonlinear refraction (NLR). A reference detector is used to account for laser power fluctuations.

The nonlinear absorption (NLA) is determined by measuring the total power incident (open aperture or OA) on the detector as the sample is scanned through the focus of a Gaussian beam. The nonlinear refraction (NLR) is determined by transforming the nonlinear phase accumulation into a change in the measured power via the use of a closed aperture (CA) placed in the far field of the sample [11–13]. We measure both NLA and NLR simultaneously by using an OA and CA line with associated detectors and beam splitters. The signals were measured with InGaAs detectors (Thorlabs PDA015C) for the NIR and PbSe detectors (Thorlabs PDA20H) for the mid-IR passed to a lock-in amplifier for digitization (Zurich Instruments HF2LI).

To fit the data we analytically solve for the field at the back of the sample in the slowly varying envelope and thin sample ($L << z_0$) approximations where L is the sample thickness and z_0 is the Rayleigh range [13]. We then Fresnel propagate to the aperture plane and integrate over all space and time for the energy on the OA detector or to the limit of the aperture for the CA detector [14,15]. The signals are then normalized to give the transmission T.

The sample is a 188 μm thick CSP crystal grown from a stoichiometric melt via the Horizontal Gradient Freeze (HGF) technique and polished on both sides [16]. The crystal was oriented so that the a and c-axes are in the plane perpendicular to the beam propagation direction. Measurements were performed with the field of the laser oriented along the a or c-axes. This allows us to examine the birefringence of the NLO properties, as well as spoils the phase matching ($\Delta k > 0$) so that power losses due to second harmonic generation (SHG) are negligible and not confused for NLA. The coherence length $L_c = \pi/\Delta k$ for our study is at most 92 μm at 5.0 μm, where Δk is the phase mismatch. The SHG generated is $\propto \mathrm{Sinc}[\Delta \mathrm{kL}/2]^2 \approx 10^{-4}$ of the phased matched case and negligible compared to measurement noise [17].

3. Results and discussion

In Fig. 2 we see the OA and CA signals for the Z-scan indicating the presence of four-photon absorption (4PA) along with positive NLR. The results of the Z-scan measurement across wavelengths and polarizations are summarized in Table 1. Measurement error bars are 20%.

Table 1. Summary of Z-scan measurements.

	a - axis		*c* - axis	
wavelength (μm)	α_4 (cm^5 /GW^3)	n_2 (cm^2/GW)	α_4 (cm^5 /GW^3)	n_2 (cm^2/GW)
1.5	5.30×10^{-6}	1.70×10^{-5}	7.80×10^{-6}	1.72×10^{-5}
2.0	2.10×10^{-6}	0.95×10^{-5}	3.80×10^{-6}	1.04×10^{-5}
3.0	$< 0.05 \times 10^{-6}$	1.39×10^{-5}	$< 0.05 \times 10^{-6}$	1.50×10^{-5}
3.5	$< 0.05 \times 10^{-6}$	1.43×10^{-5}	$< 0.05 \times 10^{-6}$	1.60×10^{-5}
4.5	$< 0.05 \times 10^{-6}$	1.05×10^{-5}	$< 0.05 \times 10^{-6}$	0.91×10^{-5}
5.0	$< 0.05 \times 10^{-6}$	1.28×10^{-5}	$< 0.05 \times 10^{-6}$	1.38×10^{-5}

Optical Materials EXPRESS

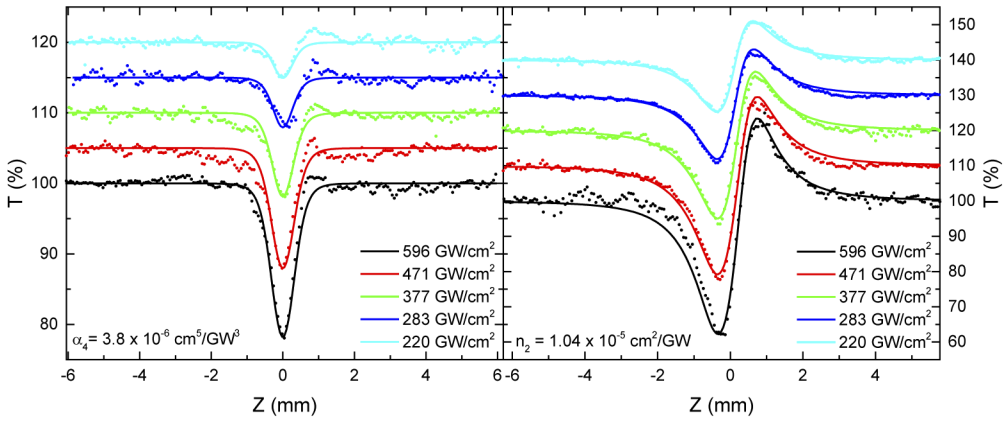

Fig. 2. Z-scans of CSP at 2.0 μm along the c-axis at various peak irradiances. Signals show normalized transmission T vs. sample position Z relative to beam focal position. Left: OA signal and fit with α_4. Right: CA signal with fit for α_4 and n_2. Plots have been shifted vertically for clarity.

To fit the OA data at NIR wavelengths the wide band gap requires us to use the 4PA coefficient α_4 such that $\alpha = \alpha_0 + \alpha_4 I^3$ where α_0 is the linear absorption coefficient and I is the irradiance. We also note that fitting with 4PA is consistent with the measured beam waist and signal scaling as a function of peak irradiance. For the MIR OA scans we find that there is no discernable NLA. We compare the measured dispersion of α_4 to the model proposed by Wherret [18] as:

$$\alpha_N[\omega] \propto \frac{1}{n^4 E_g^{11}} \left(\frac{N\hbar\omega}{E_g} - 1\right) \Big/ \left(\frac{N\hbar\omega}{E_g}\right)^{4N-3} \tag{1}$$

where n is the linear index of refraction, N is the order of the MPA and $\hbar$ is the reduced Planck constant.

As seen in Fig. 3 we find good agreement to the theoretical wavelength scaling, although we do find that the measured birefringence is larger than what is expected from theory ($\alpha_4 \approx 1/n^4$), even considering the error bars in the measurements of α_4.

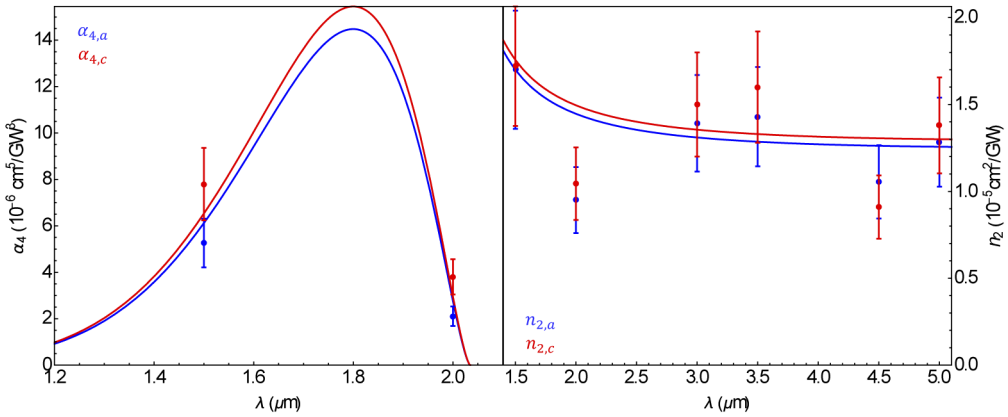

Fig. 3. Measured values of α_4 compared for a-axis (blue) and the c-axis (red) compared to the Wherrett model. Right) Measured values of n_2 for a-axis and the c-axis compared to the two band Kane model.

Optical Materials EXPRESS

For the CA scans we fit using the value of α_4 previously extracted from the OA scans as well as the second order nonlinear refraction coefficient n_2 such that $\Delta n = n_2 I$ where Δn is the index change. We compare these values to the two band Kane model for the dispersion of n_2 given as:

$$n_2[\omega] = \frac{\hbar c K \sqrt{E_p}}{n^2 E_g^4} G_2\left[\hbar\omega/E_g\right] \tag{2}$$

where $K = 3100\ \mathrm{eV}^{5/2}$ cm/GW is the Kane parameter, $E_p = 21.4$ eV is the Kane energy and G_2 is the dispersion function [19,20]. Details on the two band Kane model are given in Appendix A.

While the Kane model shows that $\alpha_4 = 0$ beyond 1 μm it does still predict n_2 into the MIR. The Kane model calculates the change in absorption due to two-photon absorption (2PA), Raman scattering and the quadratic and linear Stark effects and then calculates the associated refraction change via Kramers-Kronig relations. Hence it will still predict n_2 far beyond where 2PA is allowed due to the other effects [21,22].

As seen in Fig. 3 we find that our measurements compare well to the Kane model within the error bounds for most wavelengths. The low measurements at 2.0 & 3.5 μm are likely due to dispersion of the pulse due to atmospheric absorption. The n_2 measurements are consistent with the expected positive birefringence except at 4.5 μm. However, as the expected size of the birefringence $(1/n^2)$ is smaller than the measurement error bounds (20%) this is difficult to conclusively verify although the data trend is suggestive.

3.1. OPA performance modeling

We seek to examine the effect of the observed NLO properties on OPA performance. To do so we numerically propagate the coupled wave equations accounting for 4PA losses of the pump beam and calculate the irradiance of the generated output beams [17,23,24]. As illustrated in Fig. 4 we model the generation of a $\lambda_2 = 5.0$ μm idler using a $\lambda_3 = 2.0$ μm pump of various intensities with a $\lambda_1 = 3.3$ μm seed using the rate equations in Eqs. (3)–(5).

$$A_1' = i\frac{\omega_1 d_{\mathrm{eff}}}{n_1 c} A_3[z] A_2^*[z] e^{i\Delta k z} \tag{3}$$

$$A_2' = i\frac{\omega_2 d_{\mathrm{eff}}}{n_2 c} A_3^*[z] A_1[z] e^{i\Delta k z} \tag{4}$$

$$A_3' = i\frac{\omega_3 d_{\mathrm{eff}}}{n_3 c} A_1[z] A_2[z] e^{i\Delta k z} - \frac{1}{16} c^3 n_3^3 \alpha_4 \epsilon_0^3 A_3^7[z] \tag{5}$$

where A_j[z] is the electric field envelope of beam at position z in the crystal, ω_j is the angular frequency, n_j is the index of beam j, c is the speed of light, ϵ_0 is the permittivity of free space. The second term of Eq. (5) accounts for the NLA. The irradiance of the seed is set to $I_1 = (\lambda_3/\lambda_1) I_3 10^{-3}$. From Wei [8] the phase matching angle for Type 1 DFG (*ooe*) for a 5 μm idler is $\theta = 46.45°$ with an effective nonlinearity of $d_{\mathrm{eff}} = -d_{36}\sin[\theta]\sin[2\phi] = -61.2$ pm/V for a $\bar{4}2m$ crystal [17]. All computations are performed at $T = 300$ K.

In Fig. 5 we examine the propagation with and without 4PA. Without 4PA the pump, signal and idler continuously exchange energy as they propagate through the crystal. Where 4PA is present, it competes with the downconversion, reducing the signal and idler generated.

In Fig. 6 we calculate the conversion efficiency $\eta = I_2[L]/I_3[0]$ for a $L = 100$ μm crystal with and without 4PA under phase match for various values of α_4. With 4PA less signal and idler are generated, hence η is reduced for a given pump irradiance. Given that this much of this absorbed power will be converted to heat via non-radiative relaxation, the onset of this 4PA also increases the thermal load on the crystal, contributing to damage. We define the critical irradiance I_c as the irradiance where the normalized conversion efficiency $\eta/\eta_0 = \eta[\alpha_4]/\eta[\alpha_4 = 0]$ drops by $1/e$ ($\approx 63\%$), which occurs at $I_c = 280$ GW/cm^2 for this output wavelength.

Optical Materials EXPRESS

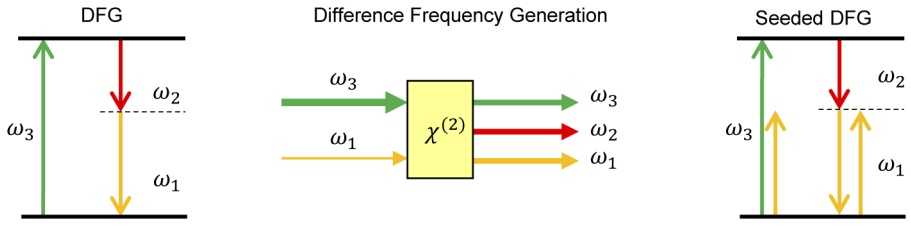

Fig. 4. Left) Difference frequency generation. The pump ω_3 is broken into two photons of lower energy, the signal ω_1 and the idler ω_2. (Center) and (Right) In our model we seed the interaction with a seed to stimulate the production of the idler.

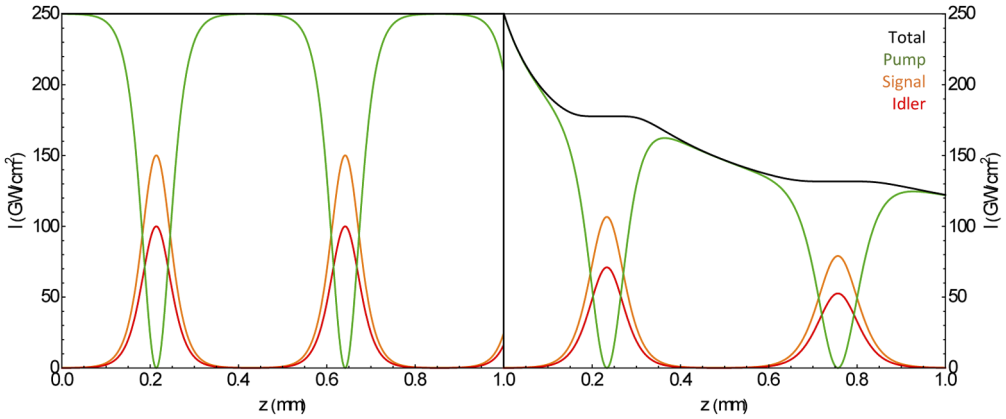

Fig. 5. (Left) Irradiances of the 3.3 μm signal (orange), 2.0 μm pump (green) and 5.0 μm idler (red) beams propagating in the crystal in absence of 4PA. The pump is set to $I_3 = 250$ GW/cm^2. The energy is continuously exchanged between the beams. (Right) In the presence of 4PA ($\alpha_4 = 3.0 \times 10^{-6}$ cm^5/GW^3) the signal and idler are reduced as the pump is attenuated.

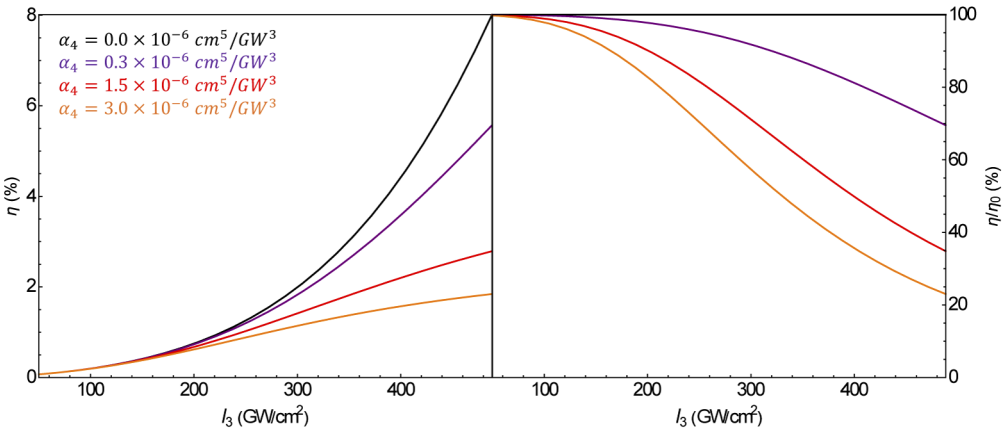

Fig. 6. (Left) Conversion efficiency for the case of a 3.3 μm signal, 2.0 μm pump and 5.0 μm idler vs. pump irradiance for a L=100 μm crystal with and without 4PA for various values of α_4. (Right) Normalized conversion efficiency η/η_0 for various values of α_4

Optical Materials EXPRESS

For the NLR, we note that the for Type I DFG the wavelengths of pump, signal and idler are governed by the relation $k_o[\lambda_1] + k_o[\lambda_2] - k_e[\lambda_3] = 0$ where k_o and k_e are the wave vectors for the ordinary and extraordinary rays at the given wavelengths [17,24]. To calculate the phase matching curves we find the signal and idler wavelengths that satisfy Eq. (6)

$$\omega_3 \left(\frac{\cos^2[\theta]}{n_o[\omega_3]^2} + \frac{\sin^2[\theta]}{n_e[\omega_3]^2} \right)^{-1/2} = \omega_1 n_o[\omega_1] + \omega_2 n_o[\omega_2] \tag{6}$$

for each value of θ under the condition that $\omega_1 + \omega_2 = \omega_3$.

Calculating the curves in Fig. 7 at low irradiance (0 GW/cm^2) and high irradiance (500 GW/cm^2) we find that the shifts in the output wavelength is less than 3 nm. This is negligible for sub-picosecond pulses, which typically have bandwidths larger than this shift (≈10 nm for a 100 fs pulse) [23,25]. The modified Sellmeier equations used to generate the curves are given in Appendix B.

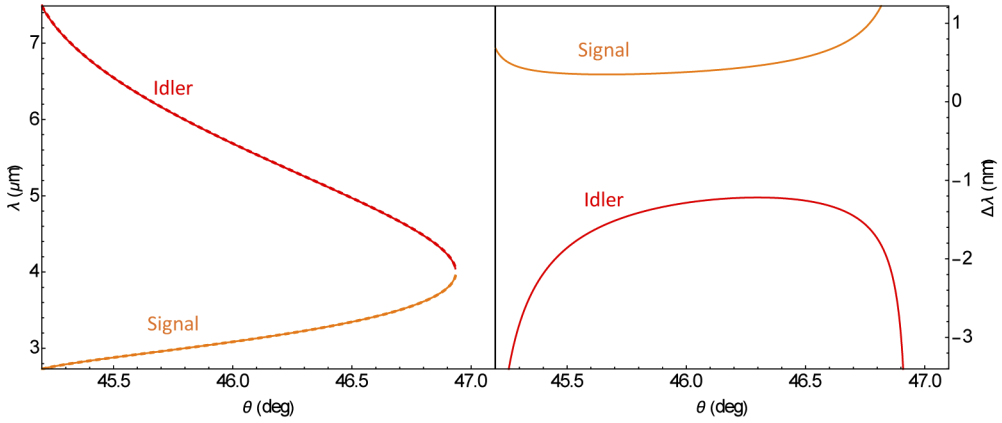

Fig. 7. Left) phase matching curves for signal (red) and idler (orange) at low (0 GW/cm^2, solid) and high (500 GW/cm^2 dashed) irradiance. The curves lie on top of each other indicating a small difference in output wavelength. Right) Difference between low and high irradiance phase matching curves

We also note that without proper cooling the additional power absorbed due to NLA can raise the crystal temperature, which would in turn adjust the phase matching angles. For the system used in our experiment focused to an irradiance of 500 GW/cm^2, the power absorption is a modest 80 mW, however a high power picosecond system could deposit tens of Watts into the crystal.

In addition we also consider the effect of the NLR on the pulse duration due to chirp. We find that for high irradiance (500 GW/cm^2) picosecond pulses this effect is negligible, and only begins to distort femtosecond pulses (100 fs) at crystal lengths longer than 1 mm, as verified through simulations using SNLO [26].

4. Conclusion

We measured the NLO properties of CSP at common pumping and MIR output wavelengths. We have determined that the dispersion of α_4 and n_2 are consistent with the Wherrett and Kane models for the NLO properties. We find that the birefringence in α_4 does have the expected sign, although the measured magnitude is larger than predicted. Due to the size of the error bars in the measurements in n_2 the sign and magnitude of the birefringence cannot be conclusively determined.

Optical Materials EXPRESS

Furthermore we have determined that α_4 can have a detrimental effect on OPA performance through absorption of pump at high irradiances like those that are present during high energy ultrafast pulse generation. This suggests that pumping irradiances in OPAs should be limited to minimize 4PA induced thermal damage. The effect of n_2 on the phase matching angles is on the order of a few nanometers and hence negligible.

Appendix A

The Kane model gives dispersion function $G_2[\hbar\omega/E_g]$ as

$$G_2[x] = G_{2,\mathrm{TPA}}[x] + G_{2,\mathrm{RAM}}[x] + G_{2,\mathrm{LSE}}[x] + G_{2,\mathrm{QSE}}[x] - G_{2,\mathrm{DIV}}[x]. \tag{7}$$

Each term corresponds to a different process contributing to n_2. $G_2[x] = G_{2,\mathrm{TPA}}$ accounts for the two-photon absorption, $G_{2,\mathrm{RAM}}$ is the Raman scattering, $G_{2,\mathrm{LSE}}$ is the linear Stark effect and $G_{2,\mathrm{QSE}}$ is the quadratic Stark effect. $G_{2,\mathrm{DIV}}$ is the low frequency divergence that needs to be removed from G_2. The equations for each of the terms are given in Eqs. (8–12)

$$\begin{aligned} G_{2,TPA}[x] &= \frac{1}{(2x)^6}\left(-\frac{3}{8}x^2(1-x)^{-1/2} + 3x(1-x)^{1/2} - 2(1-x)^{3/2}\right. \\ &\left. +2\Theta[1-2x](1-2x)^{3/2}\right) \end{aligned} \tag{8}$$

$$\begin{aligned} G_{2,\mathrm{RAM}}[x] &= \frac{1}{(2x)^6}\left(-\frac{3}{8}x^2(1+x)^{-1/2} - 3x(1+x)^{1/2}\right. \\ &\left. -2(1+x)^{3/2} + 2(1+2x)^{3/2}\right) \end{aligned} \tag{9}$$

$$G_{2,\mathrm{LSE}}[x] = \frac{1}{(2x)^6}\left(2 - (1-x)^{3/2} - (1+x)^{3/2}\right) \tag{10}$$

$$\begin{aligned} G_{2,\mathrm{QSE}}[x] &= \frac{1}{2^{10}x^5}\left((1-x)^{-1/2} - (1+x)^{-1/2} - \frac{x}{2}(1-x)^{-3/2}\right. \\ &\left. -\frac{x}{2}(1+x)^{-3)/2}\right) \end{aligned} \tag{11}$$

$$\begin{aligned} G_{2,\mathrm{DIV}}[x] &= \frac{1}{(2x)^6}\left(-2 - \frac{35x^2}{8} + \frac{x}{8}(3x-1)(1-x)^{-1/2} - 3x(1-x)^{1/2}\right. \\ &\left. +(1-x)^{3/2} + \frac{x}{8}(3x+1)(1+x)^{-1/2} + 3x(1+x)^{1/2} + (1+x)^{3/2}\right) \end{aligned} \tag{12}$$

Appendix B

The Sellmeier equations used in the computations are from Wei *et al.* [8] shown below.

$$n[T,\lambda] = \sqrt{A[T] + \frac{B[T]}{\lambda^2 - C} + \frac{D_o}{\lambda^2 - E}} + n_2[\lambda]I \tag{13}$$

The coefficients used in eqn.13 are shown in Table 2.

Table 2. Temperature dependent Sellmeier coefficients as determiend my Wei *et al.* [8].

Coef.	n_o	n_e
A	$11.95 + 5.3479\times10^{-4}T + 5.5894\times10^{-7}T^2$	$11.438 + 5.5408\times10^{-4}T + 5.0458\times10^{-7}T^2$
B	$0.6134 + 9.4768\times10^{-5}T + 2.0148\times10^{-7}T^2$	$0.61584 + 3.8668\times10^{-5}T + 2.9901\times10^{-7}T^2$
C	0.101733	0.11182
D	2334.22	2021.26
E	833.205	777.162

Optical Materials EXPRESS

Funding

Air Force Research Laboratory (#FA8650-17-F-5419).

Disclosures

The authors declare no conflicts of interest.

References

1. S. Chaitanya Kumar, A. Esteban-Martin, A. Santana, K. T. Zawilski, P. G. Schunemann, and M. Ebrahim-Zadeh, "Pump-tuned deep-infrared femtosecond optical parametric oscillator across 6-7 μm based on $CdSiP_2$," Opt. Lett. **41**(14), 3355–3358 (2016).
2. S. Chaitanya Kumar, J. Krauth, A. Steinmann, K. T. Zawilski, P. G. Schunemann, H. Giessen, and M. Ebrahim-Zadeh, "High-power femtosecond mid-infrared optical parametric oscillator at 7 μm based on $CdSiP_2$," Opt. Lett. **40**(7), 1398–1401 (2015).
3. S. C. Kumar, M. Jelinek, M. Baudisch, K. T. Zawilski, P. G. Schunemann, V. Kubecek, J. Biegert, and M. Ebrahim-Zadeh, "Tunable, high-energy, mid-infrared, picosecond optical parametric generator based on $CdSiP_2$," Opt. Express **20**(14), 15703–15709 (2012).
4. F. Hopkins, S. Guha, B. Claflin, P. Schunemann, K. Zawilski, N. Giles, and L. Halliburton, "Potential of $CdSiP_2$ for enabling mid-infrared laser sources," in *Nanophotonics and Macrophotonics for Space Environments IX*, vol. 9616 (2015), pp. 254–260.
5. T. Cooley, G. P. Anderson, G. W. Felde, M. L. Hoke, A. J. Ratkowski, J. H. Chetwynd, J. A. Gardner, S. M. Adler-Golden, M. W. Matthew, A. Berk, L. S. Bernstein, P. K. Acharya, D. Miller, and P. Lewis, "FLAASH, a MODTRAN4-based atmospheric correction algorithm, its application and validation," in *IEEE International Geoscience and Remote Sensing Symposium*, vol. 3 (2002), pp. 1414–1418.
6. A. Berk, G. Anderson, P. Acharya, L. Bernstein, L. Muratov, J. Lee, M. Fox, S. Adler-Golden, J. Chetwynd, M. Hoke, R. Lockwood, J. Gardner, T. Cooley, C. Borel, and P. Lewis, "MODTRAN5: a reformulated atmospheric band model with auxiliary species and practical multiple scattering options: update," in *Remote Sensing of Clouds and the Atmosphere IX*, vol. 5571 (2004), pp. 78–85.
7. G. Ghosh, "Sellmeier coefficients for the birefringence and refractive indices of $ZnGeP_2$ nonlinear crystal at different temperatures," Appl. Opt. **37**(7), 1205–1212 (1998).
8. J. Wei, J. M. Murray, F. K. Hopkins, D. M. Krein, K. T. Zawilski, P. G. Schunemann, and S. Guha, "Measurement of refractive indices of $CdSiP_2$ at temperatures from 90 to 450 K," Opt. Mater. Express **8**(2), 235–244 (2018).
9. K. Kato, N. Umemura, and V. Petrov, "Sellmeier and thermo-optic dispersion formulas for $CdSiP_2$," J. Appl. Phys. **109**(11), 116104 (2011).
10. V. Kemlin, B. Boulanger, V. Petrov, P. Segonds, B. Menaert, P. G. Schunneman, and K. T. Zawilski, "Nonlinear, dispersive, and phase-matching properties of the new chalcopyrite $CdSiP_2$," Opt. Mater. Express **1**(7), 1292–1300 (2011).
11. E. W. Van Stryland and M. Sheik-Bahae, *Z-Scan Measurements of Optical Nonlinearities* (Marcel Dekker, 1998), pp. 655–692.
12. M. Sheik-Bahae, A. A. Said, and E. W. Van Stryland, "High-sensitivity, single-beam n_2 measurements," Opt. Lett. **14**(17), 955–957 (1989).
13. M. Sheik-Bahae, A. A. Said, T. Wei, D. J. Hagan, and E. W. Van Stryland, "Sensitive measurement of optical nonlinearities using a single beam," IEEE J. Quantum Electron. **26**(4), 760–769 (1990).
14. B. Yao, L. Ren, and X. Hou, "Z-scan theory based on a diffraction model," J. Opt. Soc. Am. B **20**(6), 1290–1294 (2003).
15. E. Koushki, A. Farzaneh, and S. H. Mousavi, "Closed aperture Z-scan technique using the Fresnel-Kirchhoff diffraction theory for materials with high nonlinear refractions," Appl. Phys. B **99**(3), 565–570 (2010).
16. K. T. Zawilski, P. G. Schunemann, T. C. Pollak, D. E. Zelmon, N. C. Fernelius, and F. Kenneth Hopkins, "Growth and characterization of large $CdSiP_2$ single crystals," J. Cryst. Growth **312**(8), 1127–1132 (2010).
17. G. I. Stegeman and R. A. Stegeman, *Nonlinear Optics: Phenomena, Materials and Devices* (John Wiley & Sons, 2012).
18. M. P. Hasselbeck, E. W. Van Stryland, and M. Sheik-Bahae, "Scaling of four-photon absorption in InAs," J. Opt. Soc. Am. B **14**(7), 1616–1624 (1997).
19. M. Balu, J. Hales, D. J. Hagan, and E. W. Van Stryland, "Dispersion of nonlinear refraction and two-photon absorption using a white-light continuum Z-scan," Opt. Express **13**(10), 3594–3599 (2005).
20. M. Sheik-Bahae, D. C. Hutchings, D. J. Hagan, and E. W. Van Stryland, "Dispersion of bound electron nonlinear refraction in solids," IEEE J. Quantum Electron. **27**(6), 1296–1309 (1991).
21. K. Werner, M. G. Hastings, A. Schweinsberg, B. L. Wilmer, D. Austin, C. M. Wolfe, M. Kolesik, T. R. Ensley, L. Vanderhoef, A. Valenzuela, and E. Chowdhury, "Ultrafast mid-infrared high harmonic and supercontinuum generation with n_2 characterization in zinc selenide," Opt. Express **27**(3), 2867–2885 (2019).
22. T. R. Ensley and N. K. Bambha, "Ultrafast nonlinear refraction measurements of infrared transmitting materials in the mid-wave infrared," Opt. Express **27**(26), 37940–37951 (2019).

Optical Materials EXPRESS

23. B. E. Saleh and M. C. Teich, *Fundamentals of Photonics* (John Wiley & Sons, 2019).
24. P. E. Powers and J. W. Haus, *Fundamentals of Nonlinear Optics* (CRC press, 2017).
25. J.-C. Diels and W. Rudolph, *Ultrashort Laser Pulse Phenomena* (Elsevier, 2006).
26. A. V. Smith, "How to use SNLO nonlinear optics software to select nonlinear crystals and model their performance," in *Nonlinear Frequency Generation and Conversion: Materials, Devices, and Applications II*, vol. 4972 (2002), pp. 50–57.